GEOLOGOS

Geochemistry and statistical analyses of porphyry system and epithermal veins at Hizehjan in north-western Iran

Kaikhosrov Radmard[1,*], Hassan Zamanian[1], Mohamad Reza Hosseinzadeh[2], Ahmad Ahmadi Khalaji[1]

[1] Department of Geology, Faculty of Natural Sciences, Lorestan University, Khoram Abad, Iran
[2] Department of Earth Sciences, Faculty of Natural Sciences, University of Tabriz, Tabriz, Iran
*corresponding author, e-mail: k_radmard@yahoo.com

Abstract

Situated about 130 km northeast of Tabriz (northwest Iran), the Mazra'eh Shadi deposit is in the Arasbaran metallogenic belt (AAB). Intrusion of subvolcanic rocks, such as quartz monzodiorite-diorite porphyry, into Eocene volcanic and volcano-sedimentary units led to mineralisation and alteration. Mineralisation can be subdivided into a porphyry system and Au-bearing quartz veins within andesite and trachyandesite which is controlled by fault distribution. Rock samples from quartz veins show maximum values of Au (17100 ppb), Pb (21100 ppm), Ag (9.43ppm), Cu (611ppm) and Zn (333 ppm). Au is strongly correlated with Ag, Zn and Pb. In the Au-bearing quartz veins, factor group 1 indicates a strong correlation between Au, Pb, Ag, Zn and W. Factor group 2 indicates a correlation between Cu, Te, Sb and Zn, while factor group 3 comprises Mo and As. Based on Spearman correlation coefficients, Sb and Te can be very good indicator minerals for Au, Ag and Pb epithermal mineralisation in the study area. The zoning pattern shows clearly that base metals, such as Cu, Pb, Zn and Mo, occur at the deepest levels, whereas Au and Ag are found at higher elevations than base metals in boreholes in northern Mazra'eh Shadi. This observation contrasts with the typical zoning pattern caused by boiling in epithermal veins. At Mazra'eh Shadi, quartz veins containing co-existing liquid-rich and vapour-rich inclusions, as strong evidence of boiling during hydrothermal evolution, have relatively high Au grades (up to 813 ppb). In the quartz veins, Au is strongly correlated with Ag, and these elements are in the same group with Fe and S. Mineralisation of Au and Ag is a result of pyrite precipitation, boiling of hydrothermal fluids and a pH decrease.

Key words: Mazra'eh Shadi-Hizehjan, quartz monzodiorite, Spearman correlation, boiling

1. Introduction

One of the most fundamental aims in geochemical studies is to elucidate significant anomalies, determine their relationships, use correlation analyses and assess mineralisation zones so as to determine the type of exploration effectively. Most intermediate-sulfidation epithermal Au and Ag deposits are found in magmatic arcs, in calcalkaline andesitic-dacitic and more felsic rocks. A few intermediate-sulfidation deposits, typically small ones, adjoin advanced argillic lithocaps, with or without associated high-sulfidation epithermal deposits (Sillitoe, 1999). The Mazra'eh Shadi deposit is located about 130 km northeast of Tabriz (northwest Iran) in the Arasbaran metallogenic belt. Based on primary studies, such as field survey, petrographical and mineralogical investigation, the Mazra'eh Shadi region is an appropriate Cu and Au resource. Based upon a classification of structural domains of Iran (Nabavi, 1976),
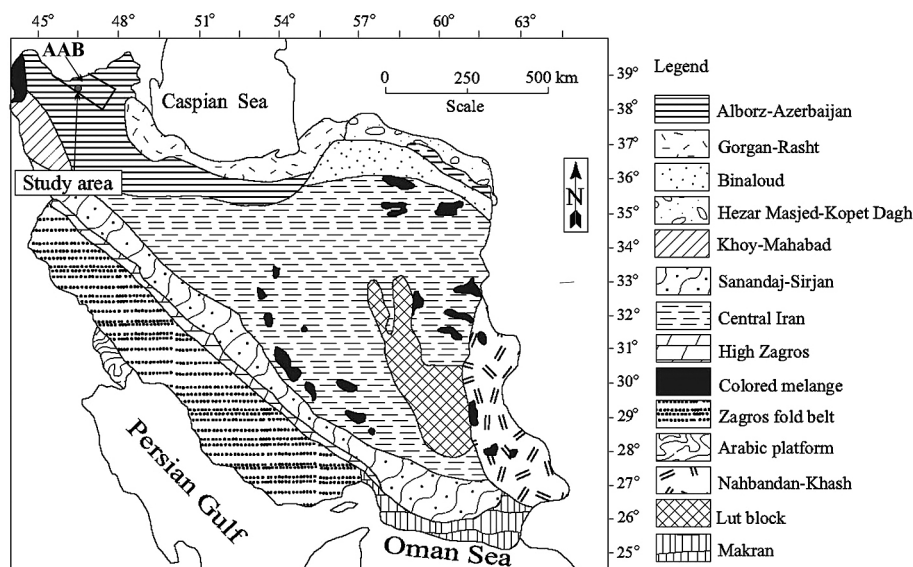
Fig. 1. Simplified regional geotectonic map of Iran (Nabavi, 1976) showing major geological-structural zones. AAB – Arasbaran metallogenic belt.

the area is part of the Alborz-Azerbaijan Zone (Fig. 1) and is located in the Ahar-Arasbaran Belt (AAB) which is characterised by a high potential of precious and base metal mineralisations. More than 10 Cu±Mo±Au porphyry deposits and epithermal gold systems have been recorded from the Arasbaran metallogenic zone (e.g., at Songon, Mazraea, Masjed Dagy, Zegleg and Darian). The purpose of the present paper is to discuss geological and geochemical data that can be used to (1) determine elemental zoning in the Arasbaran metallogenic belt, (2) provide an exploration model for epithermal deposits with characteristics similar to those of the Arasbaran metallogenic belt (3) enhance our current understanding of the processes involved in forming Au epithermal deposits. The main structure in the Arasbaran metallogenic region formed as a result of Alpine orogeny, especially of the Late Cretaceous Laramide phase.

2. Material and methods

The recent discovery of epithermal and porphyry style mineralisations in the Mazra'eh Shadi-Hizehjan region suggests that the area could potentially be productive and is in need of further investigations.

Based on previous studies more than 400 samples have been collected from surface and drill core samples in the Mazra'eh Shadi-Hizehjan region. Forty five thin and polished sections were studied by optical microscopy at Tabriz University. For determination of major rock-forming minerals in the ores, 63 samples were selected for X-ray diffraction (XRD) analysis using a SIEMENS model D-5000

diffractometer with CuKα radiation, voltage 40 kV, beam current 80 mA, continuous scanning, scanning speed 8°/min, scan range 2°–70°, slit DS = SS = 1°, ambient temperature 18°C and humidity 30% in Binalod laboratory (Iran). Rock samples were crushed to 200-mesh size particles using an agate mill. The chemical analyses were performed in the Amdel laboratory (Australia) and ALS Chemex Canada. Gold was analysed by inductively coupled plasma optical emission spectrometry (ICP-OES) and Ag, Pb, Zn, Cu, As, Sb by inductively coupled plasma mass spectrometry (ICP-MS). Detection limits for these elements were: Au=1 ppb, Ag=0.2 ppm, Pb, Zn and Cu=0.5 ppm (Tables 1–2). Ten samples containing quartz veinlets from diamond drill holes and surface samples were selected for thermometric analyses. Microthermometric studies were conducted on 100–150-µm-thick polished slabs prepared from ten quartz samples from silicified and mineralised zones. Most samples were from gold-rich and quartz-sulphide breccia veins. Ten subsurface samples containing quartz veinlets from diamond drill holes and surface samples were selected for thermometric analyses. Microthermometric studies were carried out at the Lorestan University, Geological Department–Fluid Inclusion Laboratory, using a Linkam THMSG600 freezing-heating stage mounted on an Olympus microscope. Freezing-heating stage has ±0.1 °C precision and the temperature range varies from –196 to 600 °C. In order to prevent fluid inclusions from cracking during heating, a cooling process has to be employed. Salinities of liquid-rich fluid inclusions were calculated from measured ice-melting temperatures using

Table 1. Results of chemical analyses of quartz monzodiorite. Au is in ppb; other elements are in ppm. Gold analyses were performed by fire assay, while other elements were analysed by inductively coupled plasma mass spectrometry (ICP-MS).

	Au	Pb	Ag	Cu	Zn	Mo	As	Sb	Bi	S	Sn	W	Te	Rb	K	Mn	Ti	Tl	Ni	Cd
AEI22	3	32.6	0.14	62.1	53.3	1.9	22.4	0.5	2.1	5900	1.1	0.9	0.2	31.5	7490	395	4980	1.3	3	0
MHI1	136	192	0.11	39.8	29.4	19.3	9.9	0.9	2.7	8670	5.5	7	0.5	53	18500	21	3990	3.7	0	0.5
MHI15	25	114	0.18	114	153	18.1	18.1	1.3	2.4	70000	2.6	3.7	0.6	40.4	12000	30	5560	2.3	26	3.2
MHI36	2	12.7	0.29	76.3	58.2	1.7	34.8	0.7	0.7	1430	0.4	0.4	0.5	15.4	5770	570	1970	0.3	0	0
MHI39	2	23.3	0.21	26	27.7	0.7	73.3	3.4	1.3	11700	1	1.2	1.6	37.3	13900	384	4620	1.1	0	0
MHI4	73	172	0.09	46.9	40.2	31.4	29.6	0.6	2.1	56000	3.4	3.2	1.3	55.5	20200	17	2750	3.7	13	1
MHI41	12	0	0.27	47.2	125	2.3	25.1	3.1	10.1	27000	0.7	1.7	0.8	4.7	1810	829	2950	0.2	36	0.4
MHI43	14	43.2	0.08	18.5	9.1	1.3	11.9	1.2	1.2	17600	1	1.2	0.3	29.8	11700	25	5180	1.6	3	0
MHI44	5	63.2	0.08	20.4	44.5	7.6	145	2.3	2.1	38300	1	0.6	0.8	4.4	2060	131	955	1.5	18	0
MHI46	3	0	0.1	14.3	27.2	4.1	18.4	1.2	0.4	31400	0.9	2.1	1.1	1.7	887	382	3140	0.1	5	0
MHI48	5	129	0.1	76	12	2.4	33.6	1.6	14.2	6110	0.7	0.8	1.5	18.6	7380	33	1590	0.7	0	0
MHI5	463	29	0.12	745	27.4	26.7	14.5	0.4	0.1	6520	1.6	1	0	18.5	10700	71	3920	1	8	0.1
MHI52	7	7	0.06	69.7	105	3	7.9	0.9	0.2	18500	1	0.9	0.4	20.1	6550	1530	3160	0.3	15	0.2
MHI55	3	5.3	0.2	50.9	76.2	2.2	29.4	0.7	0	28200	1.2	1.2	1.3	11	4640	680	5670	0.2	16	0.3
MHI60	31	79.8	0.09	37.1	46	87.1	12.5	1	0.3	51800	2	3.3	2	57	18500	232	2830	1.7	7	0.2
SHI3	2	8.4	0.43	390	73.3	0.7	12.9	1.5	0.5	4120	0	0.3	2.7	15.4	4320	295	950	0.2	0	0
MHI22	16	44.6	0.73	18.4	28.8	4.6	23.5	3.2	1.4	18800	1.2	2.9	0.3	413	1E+05	713	5250	6.4	6	0
MHI23	71	87	0.94	13	144	2.3	93.7	13.3	0.5	8790	0.6	1.5	0.2	310	74200	203	2980	5	2	0.7
AEI43	11	9	0.44	37.9	88.4	4.5	31.3	3.1	0.7	31300	0.9	4	1.3	113	16700	654	3700	1.3	10	0.5
KSI113	277	3130	1.39	220	981	44.3	104	25.5	0.5	3700	0.5	6.7	0.7	95.6	23500	329	2040	1.1	4	2.8
KSI28	59	51.3	1.07	143	643	24.1	106	8.8	0.9	20100	0.4	4.1	1	4.7	1370	2550	1990	0.1	18	3.2
KSI29	30	22.3	0.59	44	69.5	5	21.6	1.7	0.4	38300	0.8	1.9	1.5	101	28200	831	4310	1.2	12	0.2
KSI31	798	618	0.42	149	1650	4.6	7.2	4.2	0.3	11800	0	0.2	0.2	16.8	5340	3400	142	0.3	4	27

Table 2. Results of chemical analyses in Au-bearing quartz veins. Au is in ppb; other elements in ppm. Gold analyses were performed by fire assay, while other elements were analysed by inductively coupled plasma mass spectrometry (ICP-MS).

	Au	Pb	Ag	Cu	Zn	Mo	As	Sb	Bi	S	Sn	W	Te	Rb	K	Mn	Ti	Tl
KSI56	8	8.3	0.36	30.3	5.9	6.3	684	0.9	0.1	21100	0.9	1.9	0	5.1	6840	62	3560	0.3
KSI57	2	11	0.23	15	2.4	8.5	377	0.7	0.2	12200	0.9	1.5	0	2.9	4650	80	3030	0
KSI59	2	11.4	0.28	23.1	3.3	4.3	382	0.7	0.1	16400	1.2	1.7	0	3.3	4040	65	4280	0.9
KSI60	1	12.2	0.2	32.2	2.4	3.3	278	0.6	0.1	38600	0.8	1.4	0	4.4	13100	78	3660	0.4
KSI65	9	8	0.23	13.4	0.9	5.9	53	0.8	0.1	2250	1.1	1.3	0	1.7	1260	45	3840	0.1
KSI66	3	13.2	0.39	42.2	5.8	9	145	1	0.1	4430	1.6	1.6	0	2	1830	76	6650	1.4
KSI71	4	17.5	0.36	261	14.7	18	1820	1	0.2	5750	1	1.3	0	1.5	1480	127	4610	0.3
KSI73	3	24.8	0.32	33.3	3.2	8.5	151	1.3	0	20700	1.2	2.9	0	3.3	5990	88	5750	0.6
KSI74	5	32.5	0.23	16.7	3.7	9.2	93.1	1.1	0.6	18600	1	3.4	0	2.1	5440	33	4040	0
KSI75	895	4300	3.21	611	144	9	85.4	37.7	0.2	20100	0.5	2.1	1.3	9.1	8300	65	848	0.4
KSI77	456	3120	6.1	158	71.5	4.9	249	13.1	0.9	9630	0.6	3.2	0.9	5.5	4690	124	1880	0.5
KSI78	2420	3840	1.69	68.9	333	12.3	699	25.4	0.2	20800	0.6	6.8	0.4	25.6	8580	71	3110	7.3
KSI81	17100	21100	9.43	251	182	1.8	114	15.6	0.2	16500	0.5	4.2	0.6	4.1	5790	102	498	0.7
KSI82	122	153	0.87	8.2	10.4	2.1	28.6	1.7	0.6	18300	0.8	1.1	0.8	76.5	31300	28	2120	1.6
KSI85	29	66.6	0.73	45	7.1	3.1	17.2	1.1	0.8	2200	2	1.3	0.5	97.3	33200	61	3610	1.7
KSI87	1280	867	2.94	13.9	31.8	2	11.6	28.5	0.6	1180	0.6	0.2	0	41	12200	49	740	0.6

the equation of Bodnar (1993). Interpolation of data and creation of longitudinal sections for the veins was done using the Kriging interpolation function built in the Surfer software, version 9, Excel, Auto CAD. The basic statistics, minimum, maximum, mean and standard deviation were calculated for every vein by SPSS software, version 16.

3. Geology

In the study area three types of lithologies are represented (Radmard et al., 2017; Fig. 2), as follows:
1. Eocene pyroclastic rocks, consisting especially of tuff and lava usually of an andesitic composition;
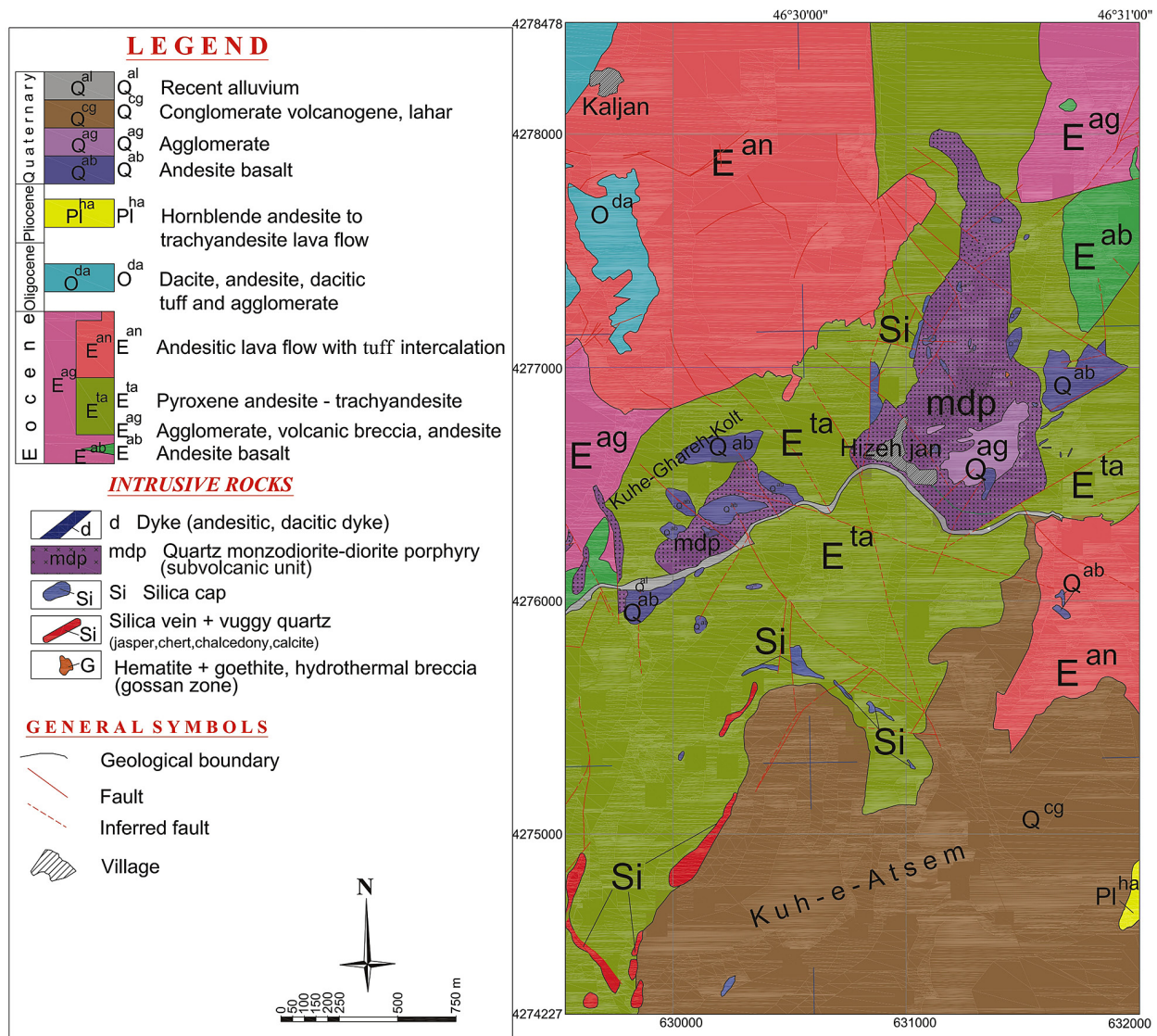
Fig. 2. Geological map of the Mazra'eh Shadi-Heizehjan region (Radmard et al., 2017).

2. Oligocene–Pliocene rocks, consisting of hornblende andesite to trachyandesite lava, dacite tuff and agglomerate;
3. Quaternary volcanogenic conglomerate (agglomerate) and alluvial units.

The Eocene pyroclastic, volcanic and agglomerate (usually of an andesitic composition) are covered by dacitic tuff, dacite, hornblende andesite, trachyandesite and andesite volcanic rocks of Oligocene and Pliocene age. Numerous dacite to andesitic dykes intruded into volcanic and pyroclastic rocks of Late Eocene age. The youngest rock units in the area are Quaternary alluvial plain and river sediments. The Quaternary volcanogenic conglomerate (agglomerate) crops out in the vicinity of the Mazra'eh Shadi deposit in the southwestern part of the study area (Fig. 2). Subvolcanic rocks such as quartz monzodiorite-diorite porphyry intruded into

Eocene volcanic and volcano-sedimentary units and caused mineralisation and alteration. Gold mineralisation in the Hizehjan area is related to Eocene volcanic and intrusive rocks. Outcrops of subvolcanic rocks extend over a distance of about 1,650 m and their width ranges from 300 to 450 m in the area.

4. Results

4.1. Alteration

Hydrothermal alteration zones are well developed around the Mazra'eh Shadi veins and Hizehjan. Hydrothermal activity and the presence of faults and highly fractured breccia zones led to a range of alteration phenomena in Mazra'eh Shadi (Radmard et al., 2017; Fig. 3). Alteration associated with
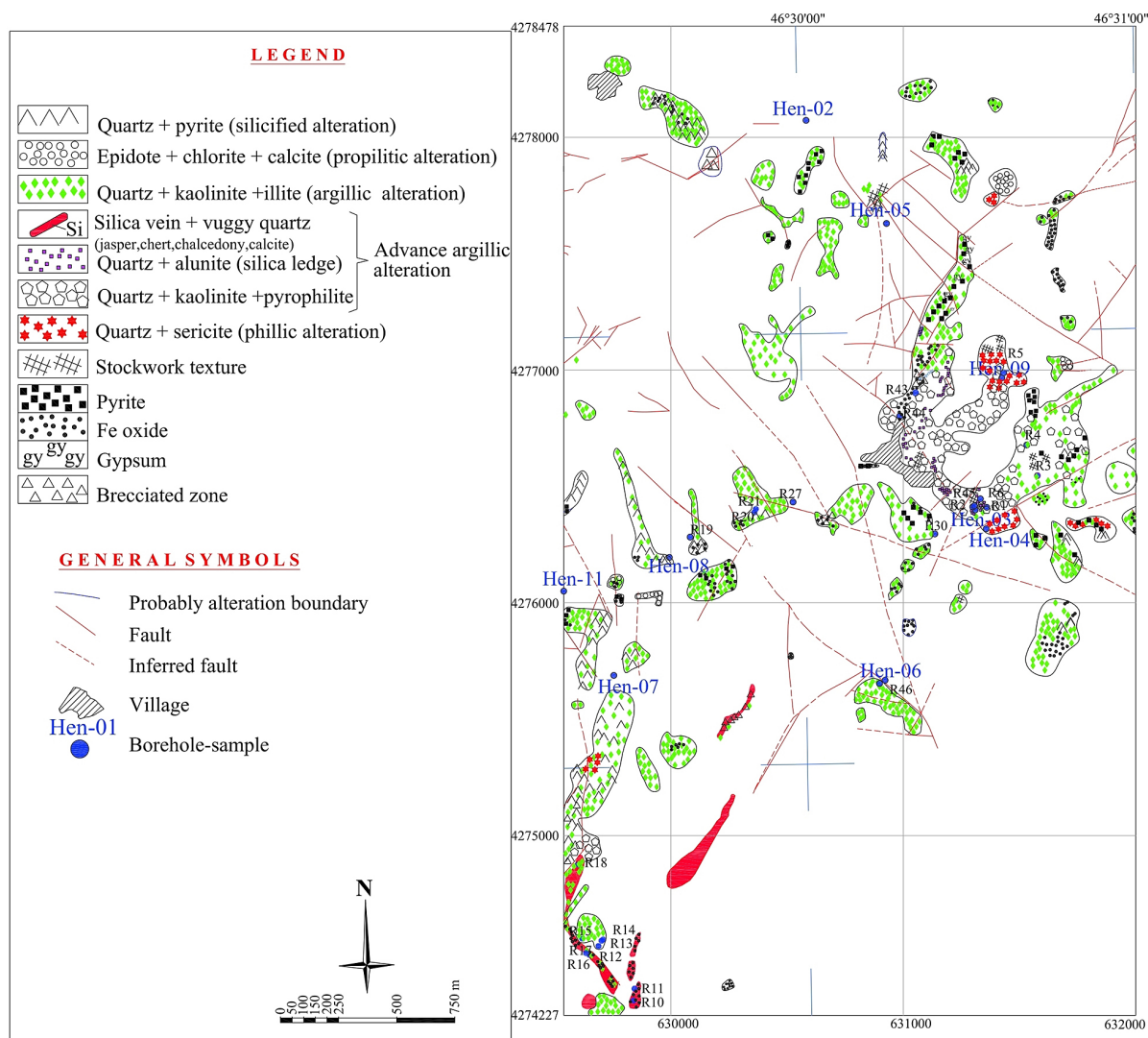
Fig. 3. Map of alteration zones in the Mazra'eh Shadi-Heizehjan region (Radmard et al., 2017).

mineralisation is confined to thin halos of silicified rocks adjacent to the veins, bordered by argillic and propylitic zones outwards. Field mapping, microscopic study and XRD analysis (Table 3) have resulted in the recognition of five, zonally distributed hydrothermal alteration assemblages that consist of propylitisation, phyllic, argillic-advanced argillic alterations and potassic associated with silicification and ore deposition.

Generally, outcrops of silicification can be divided into three main forms: stockwork in the north-

eastern part of the area; distinct silica caps at outcrops in the central and southwestern parts and quartz veins with an N 20–80°E trend in the southwestern part. The presence of several scattered and separated silica caps in argillic alteration indicates that the surface of silica caps are rough, highlighting this morphology due to their resistance to weathering (Fig. 4A).

The argillic alteration is subdivided into argillic and advanced argillic alterations. Argillic alteration is present in the central part of the area; it led to

Table 3. Minerals (identified by XRD analyses) in hydrothermal alteration zones of the Mazra'eh Shadi deposit.

Alteration zones	Major Minerals	Minor Minerals
Propylitic	chlorite, albite, calcite,	montmorillonite, calcite
Phyllic	quartz, muscovite, illite,	chlorite, kaolinite, natrojarosite, jarosite, pyrite
Argillic	quartz, kaolinite, montmorillonite	muscovite, calcite, goethite, illite, chlorite,
Advanced argillic	kaolinite, quartz, gypsum,	muscovite, illite, alunite, montmorillonite, hematite
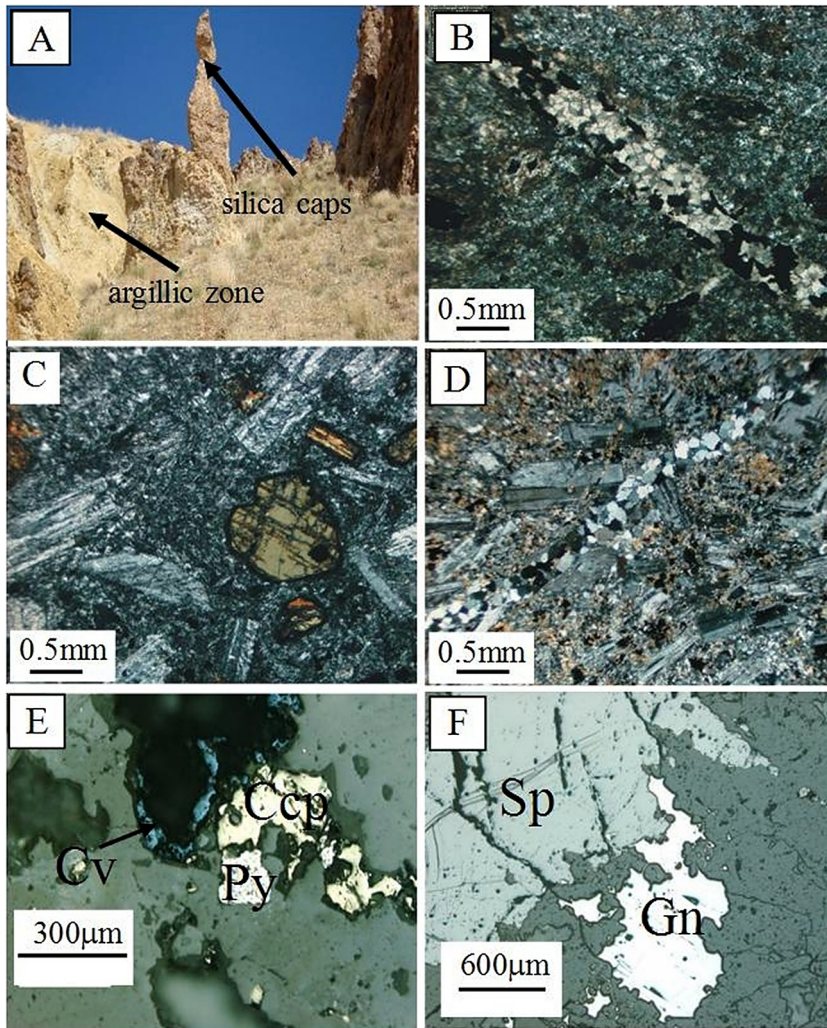
Fig. 4. A – Silica caps in argillic zone; **B** – Borehole Hen 03–105.6 m: highly to moderately phyllic-argillic alteration microporphyritic quartz diorite; **C** – Borehole Hen 07 – 161.6 m: moderately propylitic alteration in propyritic andesite. Plagioclase and hornblende microphenocrysts are major constituents of this rock; **D** – Borehole Hen 04 – 342 m: moderately potassic (biotitic) alteration. Note the parallel feldspar microphenocrysts and quartz+opaque filled vein; **E** – Paragenesis of chalcopyrite (Ccp), covellite (Cv) and pyrite (Py); **F** – Sphalerite (Sp) with galena (Gn) in quartz.

crystallisation of a quartz-kaolinite-montmorillonite-chlorite assemblage. In general, it is marked by the complete replacement of plagioclase and K-feldspar. Kaolinite and pyrophyllite are typical mineral phases of the advanced argillic alteration as a result of intense acid attack which culminated in complete leaching of alkali cations with destruction of feldspars and mafic silicate phases (Fig. 4B). XRD analyses indicate that kaolinite is the dominant phyllosilicate, accompanied by illite. Advanced argillic alteration is developed mainly in the northern and eastern parts of Hizehjan and in the northern and northwestern part of Sharafabad; it is the most widespread type in the area.

Phyllic alteration was found in drill cores in the northeastern, southeastern and southwestern parts of Hizehjan where it is more abundant than other alteration types.

Propylitic alteration is developed mainly in the southern, central and northeastern parts of the area and is seen predominantly in andesitic and trachyandesite (Fig. 4C).

Potassic alteration did not occur at rock surface and generated only in well 4 (284 m) where it has a thickness of 70 m (Fig. 4D). This type of alteration may reflect injection of a younger phase into the quartz monzodiorite.

4.2. Mineralisation

Mineralisation occurs both as a porphyry type and an epithermal type. The porphyry deposits occur exclusively along Hizehjan faults in the eastern part of the area. Geostatistical and fractal modelling (concentration-number and concentration-area fractal models) in the Hizehjan-Sharaf Abad area show that there is a direct relationship between Au mineralisations and faults (Rassi & Afzal, 2015). Mineralisation in epithermal types mainly includes Au-bearing quartz veins within andesite and trachyandesite, which is controlled by fault distribution and is restricted to quartz veins. The textural setting of ore minerals include disseminations, massive accumulations and as

Table 4. Summary of microthermometric data and calculated parameters for primary fluid inclusions in mineralised quartz from the Mazra'eh Shadi deposit.

Sample	Phases	T_{fm} °C	Tm, ice °C	Th(L+V) °C	Salinity Wt. %	Density g/cm³	Homoge- nised to	Size μm	Shape	Au (ppb)	Zn+Pb (ppm)
R-19	L+V		−0.1	308.2	0.166	0.672	L	61.1	Elongate		
R-19	L+V	−21	−1.3	178.9	2.143	0.908	L	13.9	Irregular		
R-19	V+L		−0.8	173.4	1.322	0.908	V	7.3	Irregular		
R-19	V+L		−0.7	287.1	1.158	0.733	V	15.0	Spherical		
R-19	L+V		−0.5	221.1	0.827	0.844	L	12.0	Spherical		
R-19	L+V	−26	−2.8	201.9	4.546	0.902	L	5.2	Spherical		
R-19	L+V	−23	−2.3	209.5	3.757	0.887	L	16.0	Elongate		
R-19	L+V		−1.1	178.2	1.816	0.906	V	6.1	Elongate		
R-19	L+V		−1.9	204.5	3.117	0.887	L	7.4	Spherical		
R-19	L+V	−22	−1.6	251.7	2.632	0.818	L	11.4	Spherical		
R-19	L+V	−22	−2.1	256.6	3.438	0.819	L	16.3	Spherical	59	1156
R-19	L+V		−1.4	231.2	2.306	0.844	L	11.3	Spherical		
R-19	L+V		−2.6	267.3	4.232	0.81	L	6.9	Spherical		
R-19	L+V		−2	210.4	3.278	0.881	L	9.7	Elongate		
R-19	L+V	−23	−1.8	190.5	2.956	0.9	L	11.1	Elongate		
R-19	V+L	−22	−0.9	270.0	1.487	0.771	V	12.1	Spherical		
R-19	V+L	−22	−0.4	298.3	0.662	0.702	V	31.2	Elongate		
R-19	V+L		−0.1	255.9	0.166	0.782	V	10.6	Spherical		
R-19	V+L		−0.3	259.9	0.497	0.779	V	17.2	Spherical		
R-19	V+L		−0.6	324.1	0.993	0.647	V	16.3	Elongate		
R-19	L+V	−24	−2.1	189.2	3.438	0.905	L	30.8	Spherical		
R-17	L+V	−21	−0.6	216.1	0.993	0.853	L	90.1	Elongate		
R-17	L+V	−20	−0.3	211.8	0.497	0.855	L	92.8	Elongate		
R-17	L+V		−1.1	200.3	1.816	0.881	L	10.9	Irregular		
R-17	L+V		−1.6	202.5	2.632	0.886	L	15.2	Spherical		
R-17	L+V		−0.8	192.6	1.322	0.886	L	9.8	Spherical		
R-17	L+V	−23	−2.1	238.6	3.438	0.846	L	45.0	Oval		
R-17	L+V	−25	−1.8	239.7	2.956	0.840	L	15.5	Spherical		
R-17	L+V	−21	−1.5	208.8	2.469	0.877	L	13.5	Irregular		
R-17	L+V		−1.3	160.5	2.143	0.927	L	21.7	Elongate		
R-17	L+V		−1.9	209.8	3.117	0.881	L	11.7	Elongate		
R-17	L+V	−24	−2.1	214.3	3.438	0.878	L	4.3	Spherical	2420	4173
R-17	L+V	−22	−1.5	255.6	2.469	0.809	L	27.9	Irregular		
R-17	L+V		−1.2	193.9	1.979	0.89	L	8.8	Irregular		
R-17	L+V	−22	−1.9	206.6	3.117	0.885	L	20.2	Elongate		
R-17	L+V	−23	−2.3	241.4	3.757	0.845	L	20.0	Elongate		
R-17	L+V	−21	−2.0	252.3	3.278	0.823	L	12.1	Spherical		
R-17	L+V		−1.6	176.2	2.632	0.913	L	9.6	Spherical		
R-17	L+V		−0.9	248.1	1.487	0.809	L	13.0	Spherical		
R-17	L+V	−22	−0.5	232.7	0.827	0.828	L	9.2	Spherical		
R-17	L+V		−0.3	228.1	0.497	0.83	L	11.9	Spherical		
R-17	L+V	−21	−0.9	269.5	1.487	0.773	L	13.9	Irregular		
H7-D66	L+V	−22	−1.8	209.1	2.956	0.88	L	16.5	Irregular		
H7-D66	L+V	−21	−1.3	210.6	2.143	0.871	L	20.0	Elongate		
H7-D66	L+V		−0.4	225.4	0.662	0.837	L	13.1	Spherical		
H7-D66	L+V		−0.1	221.2	0.166	0.838	L	10.6	NC		
H7-D66	L+V	−22	−1	302.3	1.651	0.709	L	10.3	Oval		
H7-D66	L+V		−0.9	236.8	1.487	0.829	L	7.5	Elongate		
H7-D66	L+V	−19	−0.5	229.7	0.827	0.832	L	18.5	Irregular		
H7-D66	L+V	−21	−0.7	226.6	1.158	0.84	L	12.2	Spherical		
H7-D66	L+V	−24	−2.1	189.9	3.438	0.905	L	10	Elongate		
H7-D66	L+V		−1.1	220.1	1.816	0.855	L	8.8	Elongate	813	389
H7-D66	L+V		−1.7	231.6	2.794	0.849	L	10.6	NC		
H7-D66	L+V	−26	−3.1	243.3	5.012	0.855	L	21.8	Elongate		
H7-D66	L+V	−21	−1.6	212.5	2.632	0.873	L	10.7	Oval		
H7-D66	L+V	−29	−3.2	222.6	5.166	0.883	L	12	Spherical		
H7-D66	L+V		−2.9	215.1	4.702	0.888	L	13.5	Elongate		
H7-D66	L+V		−1.8	220.6	2.956	0.866	L	8.2	Spherical		
H7-D66	L+V	−27	−2.5	265	4.074	0.812	L	15.8	Spherical		
H7-D66	L+V		−1.1	233.1	1.816	0.837	L	7.1	Spherical		
H7-D66	L+V	−24	−1.2	201.9	1.979	0.881	L	10.6	Elongate		

Sample	Phases	T_{fm} °C	Tm, ice °C	Th(L+V) °C	Salinity Wt. %	Density g/cm³	Homoge- nised to	Size μm	Shape	Au (ppb)	Zn+Pb (ppm)
H7-D61	L+V		–1.4	233.9	2.306	0.842	L	8.5	Spherical		
H7-D61	L+V		–0.5	252.7	0.827	0.795	L	7.1	Spherical		
H7-D61	L+V		–1.9	224.5	3.117	0.862	L	9.7	Oval		
H7-D61	L+V	–21	–0.2	244.8	0.331	0.803	L	13.3	Elongate		
H7-D61	L+V		–0.7	210.4	1.158	0.863	L	6.2	Rectangular		
H7-D61	L+V		–1	218.1	1.651	0.856	L	5.8	Spherical		
H7-D61	L+V	–20	–0.2	234.2	0.331	0.819	L	8.6	Elongate		
H7-D61	L+V	–21	–0.4	196.1	0.662	0.877	L	12.7	Elongate		
H7-D61	L+V		–0.4	213.3	0.662	0.854	L	6.4	Irregular		
H7-D61	L+V		–1.7	176.7	2.794	0.915	L	11.2	Irregular	314	589
H7-D61	L+V	–24	2.2	216	3.598	0.877	L	14.5	Spherical		
H7-D61	L+V		–1.4	221.3	2.306	0.858	L	6.6	Elongate		
H7-D61	L+V	–19	–1.3	206.2	2.143	0.857	L	6.1	Oval		
H7-D61	L+V		–0.4	219.3	0.662	0.845	L	6.6	Irregular		
H7-D61	L+V		–0.9	202.7	1.487	0.876	L	9.7	Spherical		
H7-D61	L+V		–1.5	250.9	2.469	0.817	L	6.1	Spherical		
H7-D61	L+V	–20	–0.9	219.1	1.487	0.853	L	12.1	Irregular		
H7-D61	L+V		–2.2	230.4	3.598	0.859	L	6.6	Irregular		
H7-D61	L+V		–1.3	218.5	2.143	0.861	L	6.4	Irregular		
H7-D155	L+V	–25	–1.7	233.7	2.794	0.847	L	10.8	Irregular		
H7-D155	L+V	–19	–0.5	219.3	0.827	0.847	L	8	Oval		
H7-D155	L+V		–1.5	225.5	2.469	0.855	L	7.8	Oval		
H7-D155	L+V		–0.6	259.5	0.993	0.785	L	8.5	Spherical		
H7-D155	L+V		–0.5	240.2	0.827	0.815	L	7.4	Spherical	52	1474
H7-D155	L+V	–21	–0.3	257.5	0.497	0.782	L	5.5	Spherical		
H7-D155	L+V		–0.4	280.7	0.662	0.74	L	7.9	Oval		
H7-D155	L+V	–22	–0.5	241.6	0.827	0.813	L	4.9	Elongate		
H7-D155	L+V		–0.9	260.3	1.487	0.789	L	8.7	Spherical		
H7-D155	L+V	–22	–1.2	218.8	1.979	0.859	L	8.8	Elongate		
H8-D65	L+V		–0.6	229.3	0.993	0.834	L	14.2	Spherical		
H8-D65	L+V		–0.8	261.6	1.322	0.785	L	6.6	Irregular		
H8-D65	L+V		–1.1	249.1	1.816	0.812	L	5.3	Spherical		
H8-D65	L+V		–0.5	195.5	0.827	0.879	L	29.1	Spherical		
H8-D65	L+V		–0.4	267.9	0.662	0.766	L	37	Oval		
H8-D65	L+V		–0.1	208.1	0.166	0.856	L	12.8	Elongate		
H8-D65	L+V		–0.4	251.6	0.662	0.795	L	13.8	Spherical		
H8-D65	L+V		–0.3	232.4	0.497	0.824	L	7.9	Oval		
H8-D65	L+V		–0.5	205.4	0.827	0.866	L	10.8	Elongate	70	368
H8-D65	L+V		–0.9	220.5	1.487	0.852	L	16.4	Elongate		
H8-D65	L+V		–1.4	252.1	2.306	0.812	L	6.9	Irregular		
H8-D65	L+V		–1.7	217.7	2.794	0.868	L	8.2	Elongate		
H8-D65	L+V		–0.7	193.8	1.158	0.884	L	8.7	Elongate		
H8-D65	L+V		–0.2	199.6	0.331	0.87	L	11.2	Elongate		
H8-D65	L+V		–1.5	239.4	2.469	0.834	L	24.8	Spherical		
H8-D65	L+V		–1.2	227.1	1.979	0.847	L	21.3	Spherical		
Average		–22	–1.1	227.9	1.94	0.84		14.4			
Max		–19	2.2	324.1	5.17	0.93		92.8			
Min		–29	–3.2	160.5	0.17	0.65		4.3			

a matrix of hydrothermal breccia. The main minerals of the epithermal type are galena, sphalerite, pyrite and chalcopyrite (Fig. 4E–F). Geochemical analyses of altered andesite and trachyandesite in northern Mazra'eh Shadi have demonstrated distinct anomalies of Au, Pb, Ag, Cu and Zn. Ore and gangue mineral as- semblages at Mazra'eh Shadi are typical of epithermal deposits. The superficial ore minerals are oxidised Fe-oxide/hydroxide and pyrite, whereas galena, py- rite and chalcopyrite are found in deeper horizons of the mine. The chemical analyses show maximum values of Zn (1650 ppm), Ag (1.4 ppm), Cu (745 ppm)
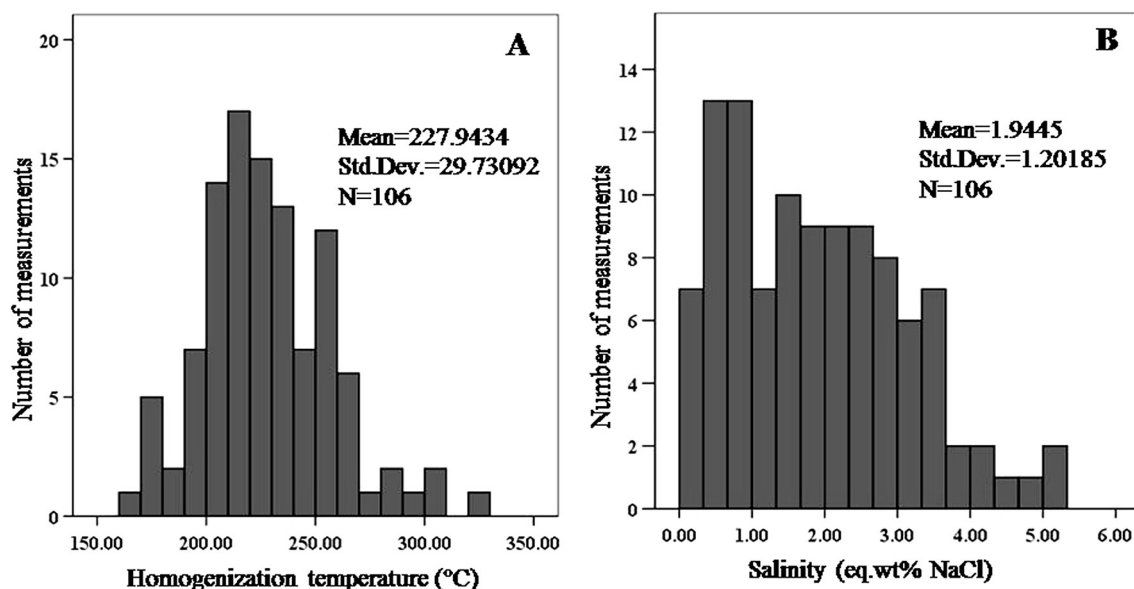
Fig. 5. Histogram of homogenisation temperature and salinity for 106 studied liquid-rich (LV) and vapour-rich (VL) fluid inclusions.

and Mo (87 ppm) in the quartz monzodiorite (Table 1). The maximum concentration of Au is 17100 ppb, of Pb it is 21100 ppm, Ag 9.43 ppm, Cu 611 ppm and Zn 333 ppm in the veins within the silicified zones (Table 2). Pyrite is the most abundant sulphide mineral. Alteration associated with mineralisation is confined to thin halos of silicified rocks adjacent to the veins, bordered by argillic and propylitic zones outwards.

4.3. Fluid inclusions

A total of 106 microthermometric measurements were performed on primary inclusions. Homogenisation temperatures of inclusions in quartz from drill core samples and surface outcrops vary be-

tween 160–324 and 176–302°C, respectively, with an average of 228°C, which were commonly observed either as inclusions along growth zones or isolated single inclusions in crystals. The ice-melting temperatures from quartz vary from 2.2 to –3.2°C, which correspond to a salinity range from 0.17 to 5.17 wt. % NaCI equivalent, with an average of 1.9 wt. % NaCI equivalent. The inclusions have a wide size range from 5 to 90 µm, with an average of 14 µm. The largest fluid inclusion in the study area has been observed in outcrop sample R17, which measures 93µm. Microthermometric data and calculated parameters such as salinities, homogenisation temperatures, ice-melting temperatures, density and size for fluid inclusions are summarised in Table 4 and graphically illustrated in Figure 5. In
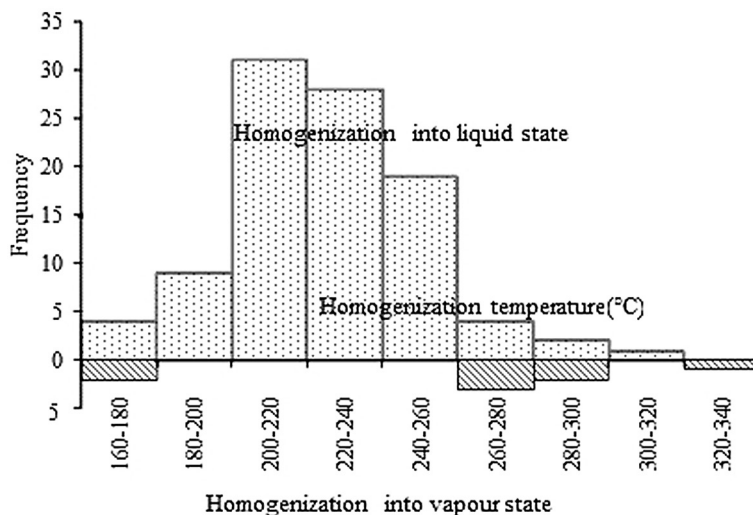

Fig. 6. Homogenisation temperature *vs.* frequency diagram in coexistence of vapour-rich and liquid-rich inclusions reflecting boiling temperature of fluid inclusion in the Mazra'eh Shadi deposit.

Mazra'eh Shadi, quartz veins containing co-existing liquid-rich and vapour-rich inclusions, as a strong evidence of boiling during hydrothermal evolution, have relatively higher gold grades (Fig. 6).

5. Discussion

In order to determine element distribution in the area, image maps were prepared for Au, Cu and other elements (Fig. 7). The surface map indicates that Au forms a strong anomaly only in one area in the southwestern region, in veins within the silicified zones. Gold mineralisation is mostly associated with Ag, as observed as veins within silicified zones in Mazra'eh Shadi. The presence of two different anomalies in Cu distribution (Fig. 7) may indicate two different phases of Cu mineralisation in the study area. Pearson correlation coefficients greater than 0.5 are significant (dependent upon the number of samples; in the present paper 0.5 for 16–23 sample), whereas Pearson correlation coefficients greater than 0.8 indicate a strong correlation between the two variables. Pearson correlation coefficients calculations and factor analysis of geochemical data were performed using the statistical package for social science (SPSS) (Nie et al., 1975). Factor analysis, which is important in the evaluation of geological studies, is a series of processes for investigating the dependence structure of multivariate models with fewer unobserved variables (Davis, 1986). The reasons that maintain the dependence among the variables are considered factors and thus their effects on the variables could be examined separately (Howarth, 1993; Tuysuz & Yaylali, 2005). Factor analysis is a statistical method that reduces numerous variables to a lesser number of mutually uncorrelated factors that can be related to similar origins or sources. Factor analysis also identifies the minimum number of variables necessary to account for the variation (% variance) in a data set (McLemore, 2008). Pearson correlation coefficients and factor analysis for quartz monzodiorite and Au-bearing quartz veins are summarised in Tables 5–8.

Statistical analyses confirm a significant correlation between Au, Ag, Pb, Zn and a strong correlation between Pb-Ag and Pb-Zn in **the** Au-bearing quartz veins (Table 6). Evidence from geology, alteration, mineralisation, geochemical investigations and grades of elements indicate that Au and Ag contents are high in quartz veins within the silicified zones in Mazra'eh Shadi (Fig. 7; Tables 3, 6–10).

Factor group 1 indicates a strong correlation between Pb, Ag, Sb and As. Factor group 2 indicates a correlation between Au, Cu and Zn, while factor group 3 consists of Mo, Sn, S and W. The placement of Au and Cu in factor group 2 can be related to similar origins or the fact that these elements were derived from the same source in a subvolcanic unit. Note that 60.07% of the variation in the data is attributed to factors 1, 2 and 3. In the Au-bearing quartz veins factor group 1 indicates a strong correlation between Au, Pb, Ag, Zn and W. Factor group 2 indicates a correlation between Cu, Te, Sb and Zn, while factor group 3 consists of Mo and As. Over 69.66% of the variation in the data is attributed to factors 1, 2 and 3. The separate associations of Au-Ag-Pb-Zn and Cu represented by factor groups 1 and 2 are confirmed by field and production data. Median and arithmetic mean for the samples are considerably different from each other and this indicates a log-normal distribution. If the distribution elements are abnormal, Spearman correlation coefficients have become more important than Pearson correlation coefficients. Based on Spearman correlation coefficients, Sb and Te can be very good indicators for Au, Ag and Pb epithermal mineralisations (Tables 9–10). The dendrogram shows that Au with Cu and Zn form the same group in quartz monzodiorite-diorite (Fig. 8). Correlation between Au and Cu indicates that these elements have similar concentrations and migrate together using the same pathway (fault) in subvolcanic units. In the Au-bearing quartz veins, Au with Zn, Fe, S, Ag and Pb forms one group (Fig. 9).

The image map for Cu, Mo, Pb, Zn, Ag, Ni, Cd and Ag*Pb*Zn/Cu*Bi*Co in subvolcanic rocks shows an irregular distribution pattern of elements (Fig. 10). Below the ore halo consists of Cu-Bi-Co, while Ag-Pb-Zn forms the upper halo. In normal conditions, from the surface into the deep this ratio must decrease. Plotting of Ag*Pb*Zn/Cu*Bi*Co of the samples against depth in borehole 3 (Fig. 11) in subvolcanic rocks elucidates two important points: the distribution pattern of this ratio is irregular, has a zigzag shape and shows higher values in the lower part. The values of Ag*Pb*Zn/Cu*Bi*Co have a range of 0.003–2.34. This diagram shows that these values are regular from the surface to a depth of 246 m and then become considerably irregular in the deeper part. It is possible that another pluton intruded within the first pluton in the region and causes the irregular shape and Ag*Pb*Zn/Cu*Bi*-Co ratio in relation to depth.

In order to illustrate element distribution in the area, we have prepared longitudinal sections for the veins using chemical assays and their corresponding "x" (Universal Transverse Mercator (UTM) easting) and "y" (elevation) co-ordinates (Fig. 12).
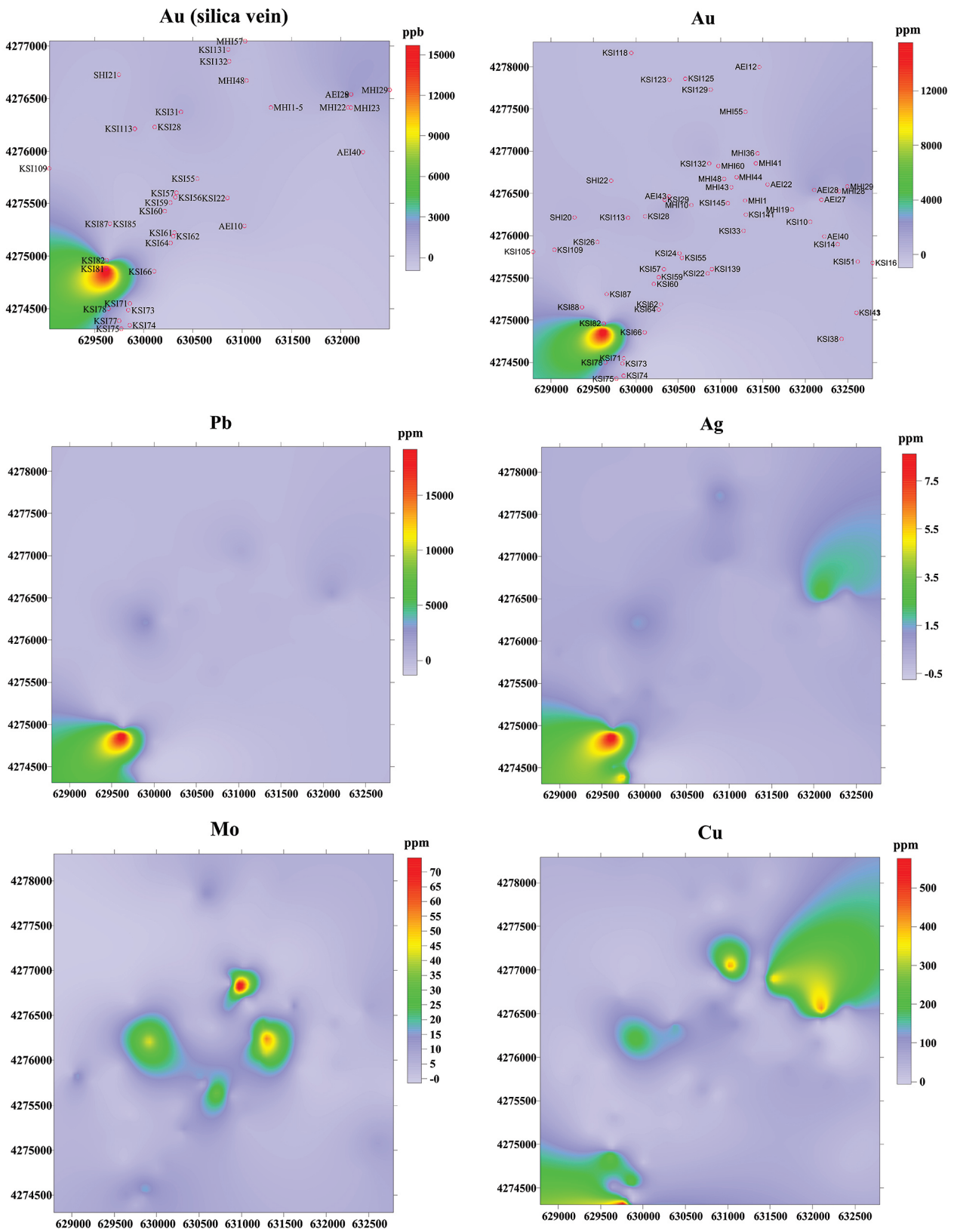
Fig. 7. Image map for Au, Pb, Ag, Mo and Cu. Axis "x" UTM easting and Axis "y" UTM northing. Location of sampled sites for Pb, Ag, Mo, Cu maps is the same as on upper right map.

Table 5. Pearson correlation coefficient values in quartz monzodiorite.

	Au	Pb	Ag	Cu	Zn	Mo	As	Sb	Bi	S	Sn	W	Te	Rb	K	Mn	Ti	Tl	Ni	Cd
Au	1																			
Pb	0.370	1																		
Ag	0.169	0.614	1																	
Cu	0.493	0.147	0.066	1																
Zn	0.786	0.581	0.501	0.129	1															
Mo	0.141	0.348	0.105	0.155	0.116	1														
As	-0.109	0.341	0.508	-0.122	0.159	0.043	1													
Sb	0.227	0.846	0.865	0.050	0.526	0.231	0.603	1												
Bi	-0.189	-0.090	-0.213	-0.153	-0.165	-0.173	-0.039	-0.116	1											
S	-0.249	-0.221	-0.275	-0.305	-0.195	0.362	-0.076	-0.281	-0.064	1										
Sn	-0.073	-0.110	-0.374	-0.103	-0.317	0.333	-0.252	-0.276	0.016	0.345	1									
W	-0.013	0.508	0.409	-0.111	0.127	0.508	0.135	0.464	-0.088	0.187	0.573	1								
Te	-0.387	-0.113	-0.072	-0.051	-0.227	0.204	-0.032	-0.145	0.097	0.233	-0.099	-0.024	1							
Rb	-0.082	0.058	0.483	-0.203	-0.079	-0.041	0.104	0.308	-0.148	-0.063	-0.005	0.194	-0.235	1						
K	-0.066	0.048	0.439	-0.179	-0.102	-0.002	0.074	0.272	-0.141	-0.054	0.058	0.187	-0.244	0.990	1					
Mn	0.523	0.033	0.303	-0.019	0.751	-0.129	-0.003	0.106	-0.177	-0.143	-0.405	-0.140	-0.170	-0.106	-0.136	1				
Ti	-0.368	-0.248	-0.192	-0.166	-0.498	-0.106	-0.319	-0.252	-0.158	0.242	0.356	0.163	-0.213	0.265	0.288	-0.374	1			
Tl	-0.100	-0.041	0.179	-0.239	-0.222	0.096	0.053	0.106	-0.082	0.139	0.464	0.336	-0.286	0.841	0.872	-0.326	0.330	1		
Ni	-0.156	-0.146	-0.064	-0.087	-0.034	0.028	0.086	-0.097	0.212	0.604	0.031	0.052	-0.058	-0.192	-0.209	0.154	0.129	-0.159	1	
Cd	0.830	0.223	0.142	0.069	0.883	-0.030	-0.112	0.128	-0.122	-0.072	-0.204	-0.119	-0.244	-0.106	-0.115	0.753	-0.429	-0.158	-0.048	1

Table 6. Pearson correlation coefficient values in Au-bearing quartz veins.

	Au	Pb	Ag	Cu	Zn	Mo	As	Sb	Bi	S	Sn	W	Te	Rb	K	Mn	Ti	Tl
Au	1																	
Pb	0.981	1																
Ag	0.820	0.885	1															
Cu	0.281	0.421	0.458	1														
Zn	0.504	0.580	0.517	0.407	1													
Mo	-0.278	-0.245	-0.338	0.280	0.179	1												
As	-0.117	-0.127	-0.198	0.163	0.084	0.757	1											
Sb	0.286	0.393	0.530	0.633	0.701	-0.012	-0.151	1										
Bi	-0.089	-0.051	0.270	-0.074	-0.056	-0.330	-0.273	-0.014	1									
S	0.063	0.090	-0.055	0.068	0.186	-0.074	-0.014	-0.075	0.133	1								
Sn	-0.373	-0.443	-0.536	-0.397	-0.516	0.028	0.028	-0.260	-0.618	-0.010	1							
W	0.417	0.472	0.369	0.128	0.826	0.269	0.088	0.312	0.590	0.034	-0.383	1						
Te	0.248	0.400	0.565	0.687	0.470	-0.186	-0.260	0.590	0.041	-0.075	0.071	-0.329	1					
Rb	-0.103	-0.131	-0.071	-0.188	-0.019	-0.402	-0.286	0.041	0.606	0.320	-0.252	-0.363	0.229	1				
K	-0.095	-0.116	-0.087	-0.164	-0.081	-0.487	-0.338	-0.035	0.541	0.071	0.027	0.336	-0.207	0.948	1			
Mn	0.272	0.325	0.421	0.355	0.181	0.371	0.549	0.022	-0.104	-0.252	-0.040	0.267	-0.224	-0.411	-0.628	1		
Ti	-0.489	-0.553	-0.698	-0.434	-0.430	0.444	0.255	-0.693	-0.403	-0.040	0.707	-0.140	0.216	-0.079	0.360	-0.426	1	
Tl	0.070	0.085	0.000	-0.097	0.763	0.211	0.124	0.330	-0.009	0.104	-0.071	0.689	0.156	0.288	0.079	0.190	-0.244	1

Table 7. Varimax rotated factor analyses (R mode) of assays of quartz monzodiorite.

	Factor 1	Factor 2	Factor 3	Factor 4
Au	0.073	0.923	–0.09	0.116
Cu	–0.105	0.675	–0.044	–0.207
Mo	0.152	0.246	0.824	–0.13
Pb	0.759	0.401	0.214	0.001
Ag	0.894	0.131	–0.035	0.066
Te	–0.039	–0.336	0.334	–0.738
Zn	0.481	0.686	–0.095	–0.057
Sb	0.954	0.188	0.049	0.07
S	–0.247	–0.282	0.628	–0.075
As	0.727	–0.252	–0.089	–0.035
Bi	–0.091	–0.309	–0.164	–0.075
W	0.427	0.027	0.71	0.349
Tl	0.088	–0.24	0.225	0.785
Sn	–0.355	–0.061	0.652	0.54
% of variance	28.67	18.20	13.2	10.47

Table 8. Varimax rotated factor analyses (R-mode) of assays of Au-bearing quartz veins.

	Factor 1	Factor 2	Factor 3	Factor 4
Au	0.969	0.085	–0.109	0.052
Cu	0.179	0.775	0.255	–0.043
Mo	–0.186	0.103	0.942	0.02
Pb	0.944	0.247	–0.103	0.062
Te	0.146	0.846	–0.267	–0.092
Ag	0.798	0.458	–0.244	–0.13
Sb	0.223	0.848	–0.029	0.056
S	–0.039	0.07	–0.117	0.918
As	–0.039	–0.044	0.875	–0.009
Bi	–0.101	0.322	–0.44	–0.552
Sn	–0.302	–0.579	0.019	–0.437
W	0.51	0.269	0.265	0.427
Zn	0.533	0.584	0.233	0.306
% of variance	38.83	18.34	12.49	9.5
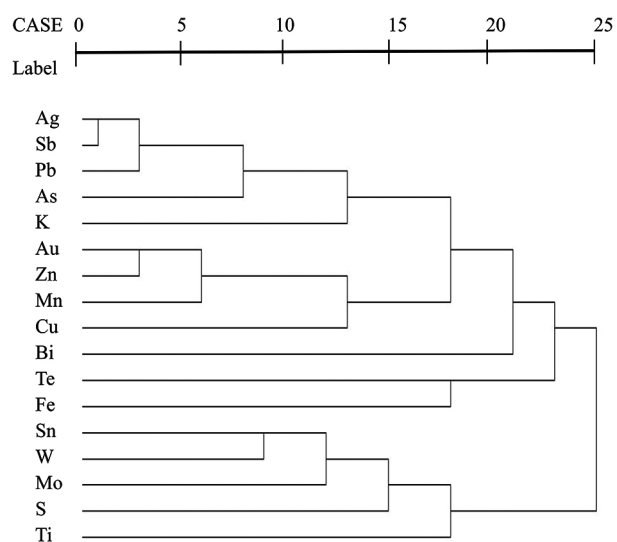
Fig. 8. Dendrogram using Average Linkage (Between Groups) in subvolcanic rocks. Rescaled Distance Cluster Combine.
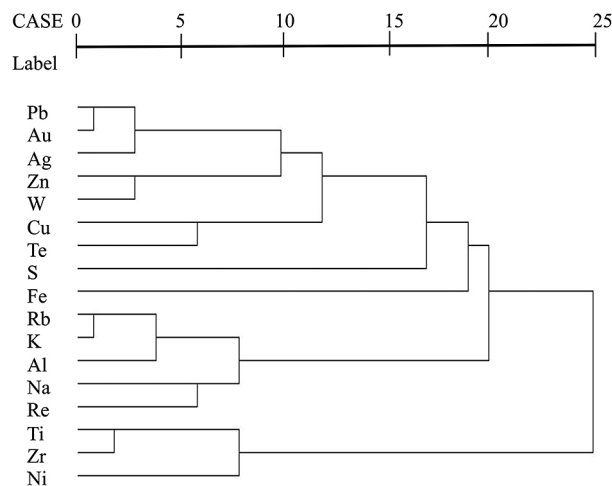
Fig. 9. Dendrogram using Average Linkage (Between Groups) in Au-bearing quartz veins. Rescaled Distance Cluster Combine.
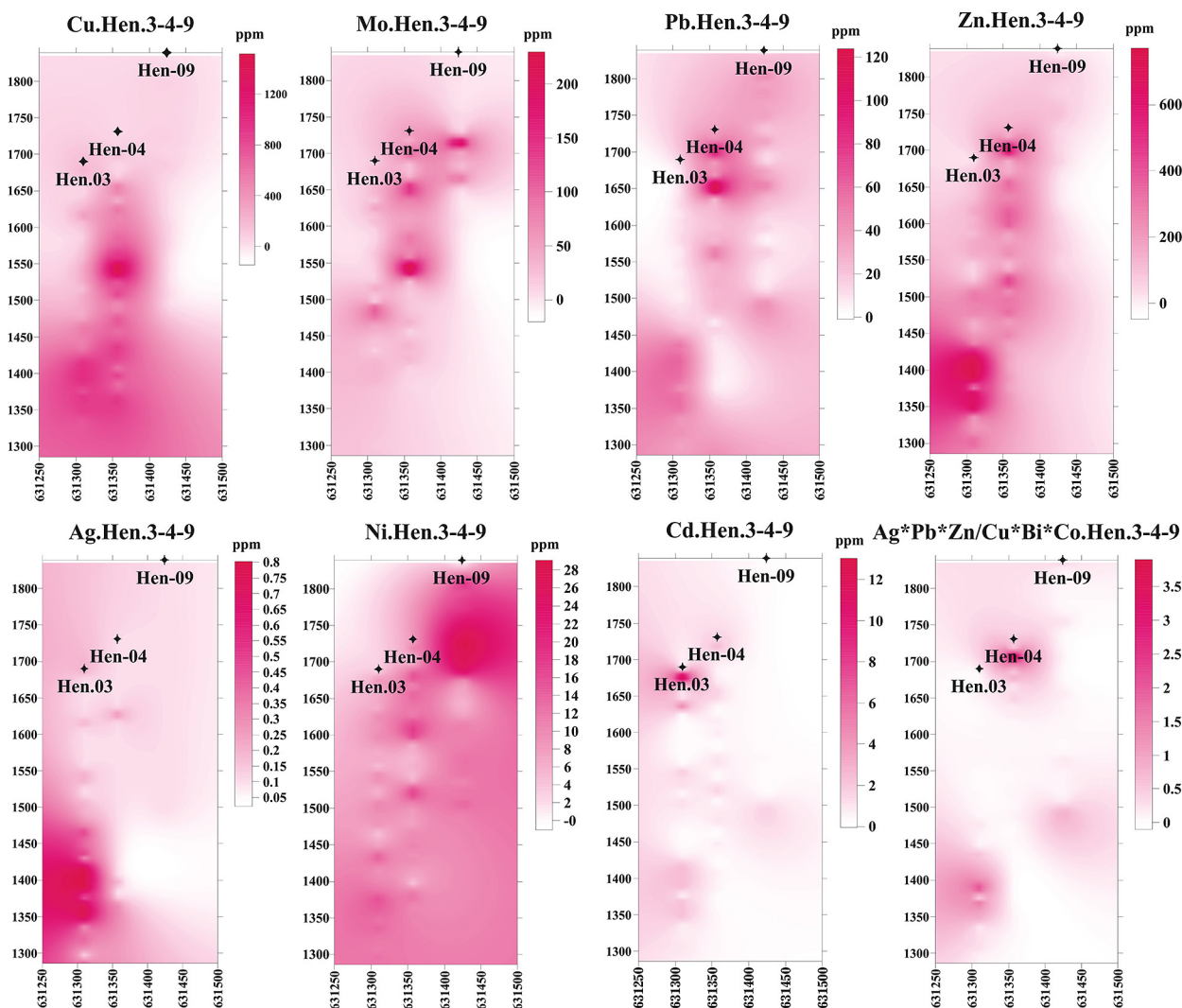
Fig. 10. Image map for Cu, Mo, Pb, Zn, Ag, Ni, Cd and Ag*Pb*Zn/ Cu*Bi* Co in subvolcanic rocks. Elevation in metres above sea level (m a.s.l.) and distance is in metres.
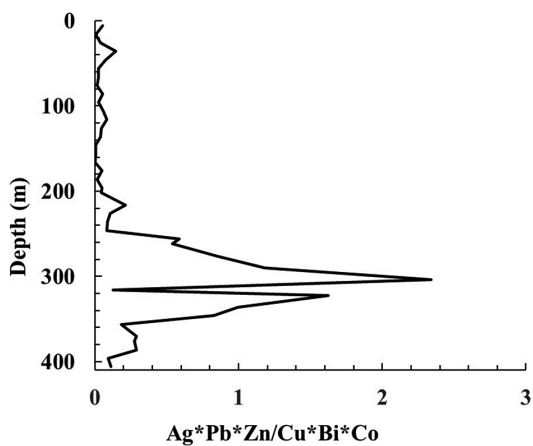
Fig. 11. Plotting of Ag*Pb*Zn/Cu*Bi*Co of samples against depth in borehole 3 in subvolcanic rocks.

Variations in metal concentrations and metal ratios occur in Mazra'eh Shadi with depth. These variations are evidence of geochemical zoning. Longitudinal sections demonstrate that Cu, Pb, Zn and Mo are concentrated at depth, whereas Au and Ag occur at shallower levels, above the base metal zones. This observation contradicts the typical zoning pattern caused by boiling in epithermal veins (Buchanan, 1981; Grancea et al., 2002). In the Purisima-Colon vein system (Pachuca, Mexico), base metals are concentrated at depth, and there is an intermediate-depth zone with high Ag grades overlapping the base metal zone (Dreier, 2005). The presence of adularia, bladed calcite, and coexisting liquid-rich and vapour-rich inclusions are evidence of local boiling (Browne & Ellis, 1970; Browne, 1978; Hedenquist et al., 2000; Simmons & Browne, 2000). Plotting of Pb, Zn and Au against depth in Au-bearing quartz veins

Table 9. Spearman correlation coefficient values in quartz monzodiorite.

	Au	Pb	Ag	Cu	Zn	Mo	As	Sb	Bi	S	Sn	W	Te	Rb	K	Mn
Au	1.000															
Pb	0.663	1.000														
Ag	0.177	0.050	1.000													
Cu	0.164	0.119	0.205	1.000												
Zn	0.281	0.110	0.564	0.421	1.000											
Mo	0.757	0.555	-0.015	0.149	0.159	1.000										
As	-0.190	0.076	0.387	-0.121	0.117	-0.006	1.000									
Sb	0.197	0.249	0.646	-0.136	0.449	0.030	0.424	1.000								
Bi	-0.114	0.300	-0.104	-0.162	-0.216	-0.066	0.285	0.104	1.000							
S	0.125	-0.077	-0.271	-0.399	0.038	0.401	-0.053	-0.020	0.009	1.000						
Sn	0.152	0.129	-0.554	-0.292	-0.438	0.350	-0.278	-0.577	0.165	0.436	1.000					
W	0.450	0.250	0.238	-0.223	0.131	0.592	0.127	0.197	0.173	0.388	0.369	1.000				
Te	-0.390	-0.213	-0.014	-0.062	-0.108	-0.026	0.212	0.089	0.040	0.323	-0.068	0.148	1.000			
Rb	0.391	0.405	0.285	-0.279	0.039	0.256	-0.024	0.189	0.051	0.047	0.294	0.470	-0.065	1.000		
K	0.441	0.464	0.224	-0.292	-0.075	0.304	0.006	0.122	0.053	0.024	0.365	0.445	-0.094	0.967	1.000	
Mn	-0.133	-0.432	0.473	0.151	0.512	-0.176	0.022	0.343	-0.385	-0.001	-0.495	-0.148	-0.023	-0.168	-0.282	1.000

Table 10. Spearman correlation coefficient values in Au-bearing quartz veins.

|	Au	Pb	Ag	Cu	Zn	Mo	As	Sb	Bi	S	Sn	W	Te	Rb	Ni	Ca	Cd
Au	1.000																
Pb	0.782	1.000															
Ag	0.847	0.837	1.000														
Cu	0.272	0.518	0.505	1.000													
Zn	0.831	0.862	0.911	0.597	1.000												
Mo	-0.235	-0.150	-0.253	0.320	-0.020	1.000											
As	-0.386	-0.303	-0.251	0.326	-0.025	0.527	1.000										
Sb	0.863	0.906	0.853	0.373	0.834	-0.058	-0.394	1.000									
Bi	0.545	0.587	0.505	0.073	0.534	-0.212	-0.401	0.506	1.000								
S	-0.135	0.035	-0.177	0.132	0.001	0.224	0.450	-0.043	-0.377	1.000							
Sn	-0.637	-0.637	-0.577	-0.250	-0.643	0.188	0.018	-0.591	-0.335	-0.311	1.000						
W	0.216	0.369	0.222	0.490	0.323	0.346	0.389	0.281	-0.092	0.540	-0.285	1.000					
Te	0.689	0.772	0.767	0.455	0.698	-0.233	-0.294	0.668	0.571	0.059	-0.550	0.253	1.000				
Rb	0.556	0.562	0.564	0.025	0.520	-0.497	-0.383	0.548	0.513	0.107	-0.407	-0.081	0.627	1.000			
Ni	-0.729	-0.731	-0.571	-0.143	-0.644	0.193	0.458	-0.678	-0.761	0.239	0.388	0.018	-0.666	-0.648	1.000		
Ca	-0.256	-0.091	-0.090	0.356	-0.016	0.158	0.476	-0.184	-0.015	0.394	0.007	0.183	-0.007	-0.049	0.391	1.000	
Cd	0.629	0.559	0.656	0.628	0.775	0.154	0.332	0.544	0.246	0.145	-0.750	0.448	0.462	0.172	-0.285	0.195	1.000
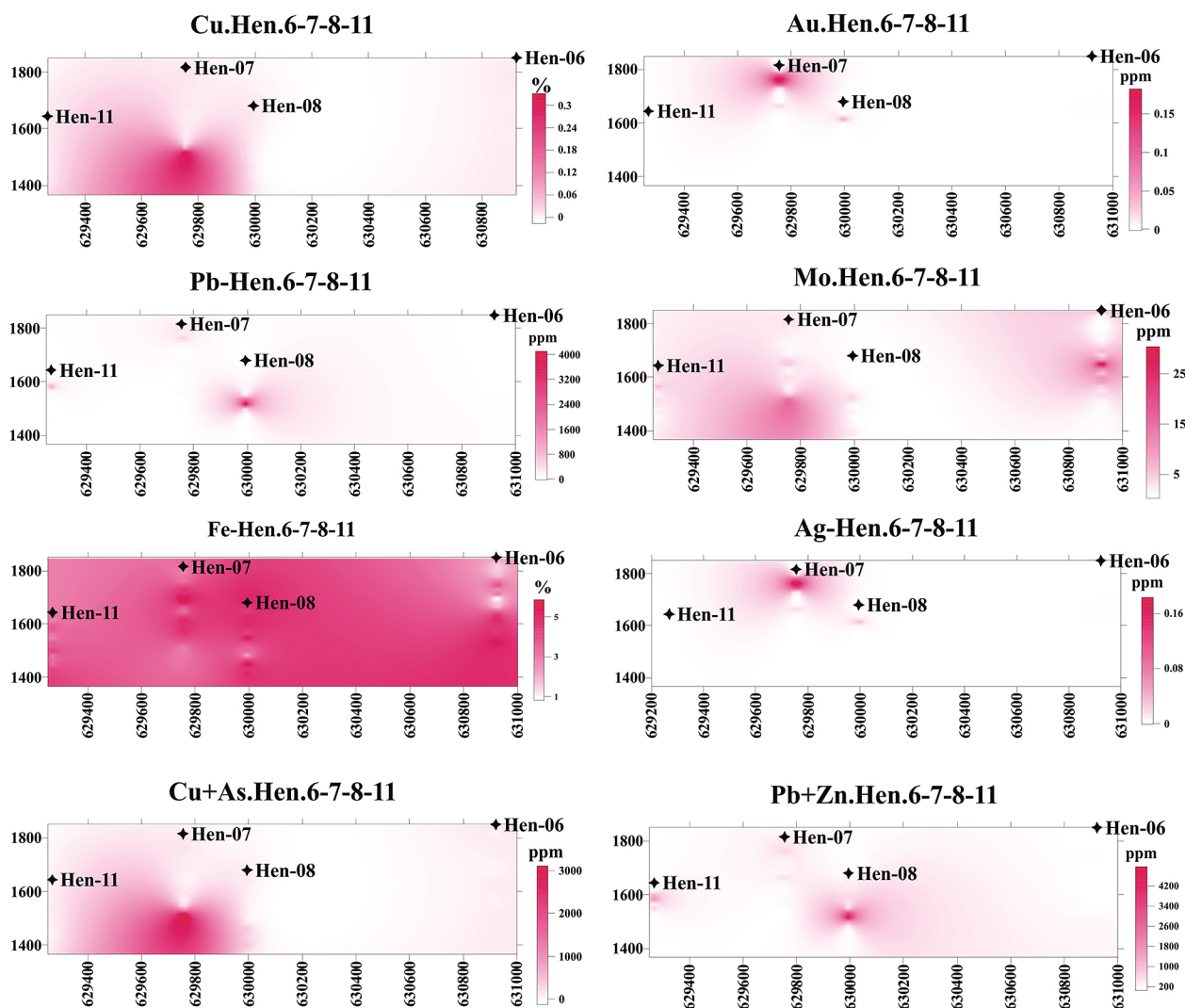
Fig. 12. Image map for Cu, Au, Pb, Mo, Fe, Ag, Cu+ As and Pb+ Zn in Au-bearing quartz veins. Axis "x" UTM easting and axis "y" elevation in metres above sea level (m a.s.l.).

shows that these elements have similar behaviours. Gold and silver concentrations increased with depth to the 45- and 155-m-levels (Fig. 13). The highest Au and Ag concentration in the study area was obtained from the phyllic-silicic alteration (Fig. 14).

In most epithermal deposits, pyrite or an iron oxide phase and adularia are common gangue minerals (Sillitoe & Hedenquist, 2003). Pyrite precipitation also promotes Au deposition by removing the complexing agent (S) responsible for Au transportation (Henley & Brown, 1985) according to equation (1)

$$Fe^{2+}+2Au(HS)^{2-} = 2Au(s)+FeS_2(s)+2H^++2HS^- \quad (1)$$
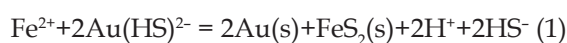
Most epithermal ore-forming fluids probably are not saturated in Au initially, but rather achieve saturation and deposit Au as a result of changes in chemical and physical conditions at the site of

deposition. In summary, precipitation of Au takes place in response to changes in temperature, pressure, pH, Eh and the activity of reduced S. The mechanisms by which Ag is dissolved and transported in epithermal systems, on the other hand, are not as well understood. If Ag is transported as a sulphide complex, boiling should also cause Ag to precipitate. However, if Ag is transported as a chloride complex boiling is less likely to result in Ag precipitation. Recent experimental studies by Pokrovski et al. (2008) at 350–500° C (temperatures somewhat higher than those in epithermal environments) have shown that the solubility of Ag in chloride solutions decreases with increasing pH, reflecting a change from transport as a chloride complex in acidic solutions to transport as S-complexes in neutral to basic solutions. Thus, the changes in solution properties described above as
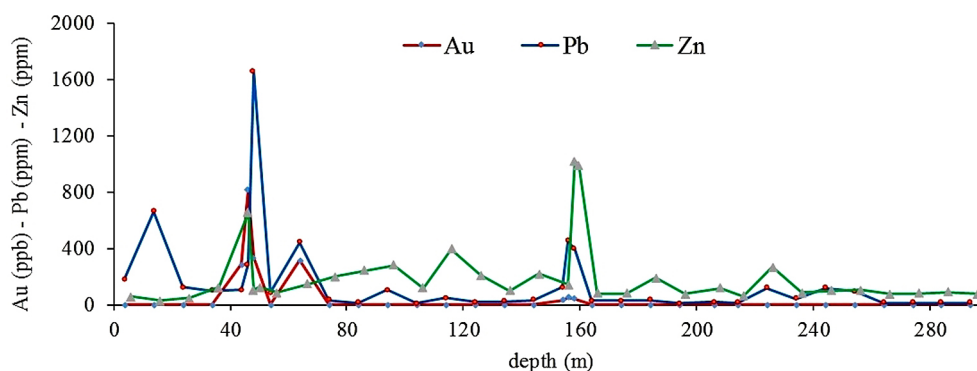
Fig. 13. Distribution pattern of Au, Pb and Zn of ore samples against depth in borehole 7 in Au-bearing quartz veins.
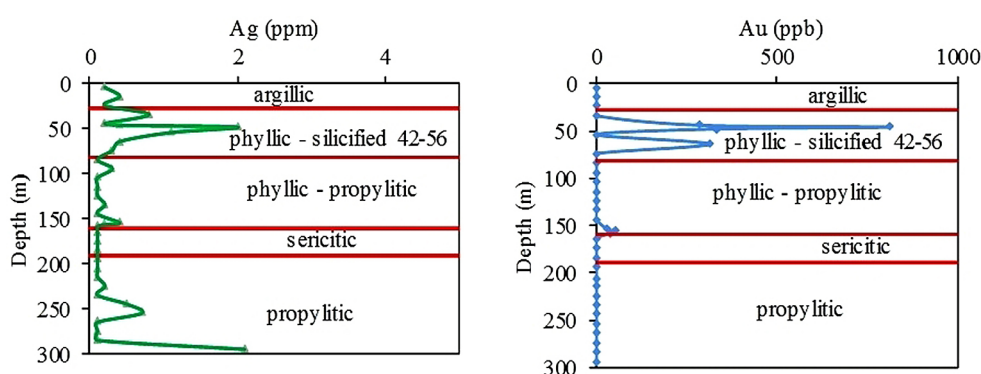

Fig. 14. Plotting of Ag and Au against depth in borehole 7 in Au-bearing quartz veins.

a result of boiling, specifically a change in pH, will also promote Ag deposition if Ag is transported as a sulphur complex. The correlation between Au-Ag and the close association of this element in a dendrogram with Fe and S in Au-bearing quartz veins (Fig. 9) are due to deposition of this element as a result of pyrite precipitation under temperatures lower than 350°C.

Silicification is also pervasive in the shallower environment where it develops as a result of cooling and decreasing acidity of hydrothermal fluids as a result water-rock interaction and mixing with surface waters (Sillitoe, 1999). The silicified zones in the Mazra'eh Shadi mining districts are surrounded by argillic alteration halos. Both Barnes (1979) and Krauskopf (1979) showed that there was evidence to suggest that chloride complexes were more stable than sulphide complexes at higher temperatures (above 350°C). The greater stability of chloride complexes at higher temperatures with respect to sulphide complexing is corroborated by the modelling studies of Ag/Au ratios in hydrothermal solutions by Cole & Drummond (1986). They found that $AuCl^{-2}$ complexes predominate at temperatures higher than 250°C and low to moderate pH, thus favouring high Ag/Au ratios in the solution. At temperatures below 250°C sulphide complexes with more Au than Ag predominate, leading to lower Ag/Au ratios in the solution.

According to Barnes (1979), deposition of metals from sulphide complexes depends on the following factors: 1) Pressure release and boiling; 2) Oxidation, decreasing the sulphide contents and pH. Thus, oxidation within and above the zone of boiling results in the formation of sulphuric acid (H_2SO_4), a pH decrease and acid leaching (argillic alteration). During this process, electrons are released that reduce the Au^+ to its neutral state Au^0 causing its precipitation as a native metal. Other important mechanisms for the precipitation of the dissolved constituents are chemical reactions between the solutions and wall rocks. Mineralisation of Au in Mazra'eh Shadi deposits due to pyrite precipitation, boiling of hydrothermal fluids and decreasing of pH.

6. Conclusions

The main results of the present study are the following:

– Statistical analyses confirm a significant correlation between Au, Ag, Pb, Zn, and a strong correlation between Pb-Ag and Pb-Zn in Au-bearing quartz veins.

– It is possible that another pluton intruded within the first pluton in the region and caused the irregular shape and Ag*Pb*Zn/Cu*Bi*Co ratio against depth.

– The longitudinal sections show clearly that Cu, Pb, Zn and Mo occur at lower elevations, whereas Au and Ag seem to occur at shallower levels. This observation contradicts the typical zoning pattern caused by boiling in epithermal veins.

– Correlation between Au-Ag and closest association this element in dendrogram with Fe and S in Au-bearing quartz veins are due deposition this element as a result of pyrite precipitation in temperatures < 350°C.

– Mineralisation of Au and Ag in the Mazra'eh Shadi deposit is due to pyrite precipitation, boiling of hydrothermal fluids and decreasing of pH.

Acknowledgements

References

Barnes, H.L., 1979. Solubilities of ore minerals. [In:] H.L, Barnes (Ed). *Geochemistry of hydrothermal ore deposits*, 2ⁿᵈ ed. John Wiley & Sons, New York. pp 404–410.

Bodnar, R.J., 1993. Revised equation and table for determining the freezing point depression of H_2O–NaCl solutions. *Geochimca et Cosmochimica Acta* 57, 683–684.

Browne, P.R.L., 1978. Hydrothermal alteration in active geothermal fields. *Annual Reviews of Earth and Planetary Science* 6, 229–250.

Browne, P.R.L. & Ellis., A.J., 1970. The Ohaki-Broadlands hydrothermal area, New Zealand: Mineralogy and related geochemistry. *American Journal of Science* 269, 97–131.

Buchanan, L.J., 1981. Precious Metal Deposits Associated with Volcanic Environments in the Southwest: In Relations of Tectonics to Ore Deposits in the Southern Cordillera. *Geological Society of Arizona, Digest* 14, 237–262.

Cole, D.R. & Drummond, S.E., 1986. The effect of transport and boiling on Ag/Au ratios in hydrothermal solutions: a preliminary assessment and possible implications for the formation of epithermal precious metal ore deposits. *Journal of Geochemical Exploration* 25, 45–79.

Davis, C., 1986. *Statistics and Data Analysis in Geology*. John Wiley & Sons, New York. 640 pp.

Dreier, J.E., 2005. The Environment of vein Formation and Ore Deposition in the Purisima-Colon Vein System, Pachuca Real del Monte District, Hidalgo, Mexico. *Economic Geology* 100, 1325 – 1347.

Grancea, L., Bailey, L., Leroy, J., Banks, D., Marcoux, E., Milési, J.P., Cuney, M., André, A.S., Istvan, D. & Fabre, C., 2002. Fluid evolution in the Baia Mare epithermal gold/polymetallic district, Inner Carpathians, Romani. *Mineral Deposita* 37, 630–647.

Hedenquist, J.W., Arribas, A.R. & Gonzalez-Urien, E., 2000. Exploration for epithermal gold deposits. *Reviews in Economic Geology* 13, 245–277.

Henley, R.W., Brown, K.L., 1985. A practical guide to the thermodynamics of geothermal fluids and hydrothermal ore deposits. *Reviews in Economic Geology* 2, 25–44.

Howarth, R.I., 1993. Statistics and Data Analysis in Geochimical Prospecting. [In:] G.J.S, Govett (Ed). *Handbook of Exploration Geochemistry*. Elsever, Amsterdam. 2, 44–75.

Krauskopf, K.B., 1979. *Introduction to geochemistry*. 2ⁿᵈ ed. McGraw-Hill Kogakushu, New York. 617pp.

McLemore, V.T., 2008. Geochemistry and statistical analyses of epithermal veins at the Carlisle and Center mines, Steeple Rock District. New Mexico, USA. *Arizona Geological Society Digest* 22, 485–496.

Nabavi, M., 1976. *An Introduction to the Geology of Iran*. Geological Society of Iran, Teheran. (in Persian). 109 pp.

Nie, N.H., Hull, C.H. & Jenkins, J.G., Steinbrenner, K. & Bent, P.H., 1975. *Statistical package for the Social Sciences*. McGraw-Hill Book Co, New York, 675 pp.

Pokrovski, G.S., Borisova, Yu.A. & Harrichoury, J.C., 2008. The effect of sulfur on vapor- liquid fractionation of metals in hydrothermal systems. *Earth and Planetary Science Letters* 266, 345–362.

Radmard, K., Zamanian, H., Hosseinzadeh, M.R. & Ahmadi Khalaj, A., 2017. Geochemistry and hydrothermal evolution of the Mazraeh Shadi–Hizehjan precious and base metal deposit, northeastern Tabriz, Iran. *Journal of Mineralogy and Geochemistry* 194-3, 227–250.

Rassi, R. & Afzal, P., 2015. Correlation between Au Lithogeochemical Anomalies and Fault-density using Geostatistical and Fractal Modeling in Sharaf Abad-Hizehjan Area, NW Iran. *Universal Journal of Geoscience* 3, 51–58.

Sillitoe, R.H., 1999. Styles of high-sulfidation gold, silver and copper mineralization in porphyry and epithermal environments. [In:] Weber, G. (Ed.): *Pacrim '99 Congress, Bali, Indonesia. Proceedings.* Australasian Institute of Mining and Metallurgy, Parkville, 29–44.

Sillitoe, R.H. & Hedenquist, J.W., 2003. Linkage between volcanotectonic settings, ore-fluid compositions, and epithermal precious- metal deposits. *Society of Economic Geologist, Special Publication* 10, 315–343.

Simmons, S.F. & Browne, P.R.L., 2000. Hydrothermal minerals and precious metals in the Broadlands-Ohaaki geothermal system: Implications for understanding low-sulfidation epithermal environments. *Economic Geology* 95, 971–999.

Tuysuz, N. & Yaylali, G., 2005. Geostatistics. *Karadenis Technical University Publication* 220, 400 pp.